Journal of Porous Materials (2020) 27:1455–1466
https://doi.org/10.1007/s10934-020-00920-1

Instant exactness synthesis and n-heptane hydroisomerization of high performance Ni/SAPO-11 catalyst

Zhishuai Yuan[1] · **Yuchun Cheng**[2] · **Shoutao Ma**[1] · **Zhen Jiang**[1] · **Yisi Zhou**[1] · **Yingjun Wang**[1] · **Wei Zhang**[1] · **Yanhua Suo**[1]

Abstract

A new method called Instant Exactness Synthesis (IES), which was applied to prepare SAPO-11 molecular sieve, was introduced innovatively. The metal–acid bifunctional Ni/SAPO-11-IES catalyst with a Ni content of 4% was prepared by the impregnation method. Ni/SAPO-11-H catalyst was prepared as a comparative sample through the traditional hydrothermal method. In addition, the growth mechanism was used to explain the excellent performance of catalyst prepared by IES method in detail. The structure of Ni/SAPO-11-IES was confirmed via XRD and TEM characterization. The pore structure of the molecular sieve was determined by nitrogen adsorption and desorption. ^{29}Si MAS NMR measurement was used to illustrate multiple silicon environment which supported the excellent acidity in NH_3-TPD measurement. Furthermore, the favourable dispersibility of Ni species was proved by the mapping of the elements and EDS. Benefiting from the superior performance of materials, Ni/SAPO-11-IES catalyst exhibited a higher catalytic performance for n-heptane hydroisomerization with n-heptane conversion of 82% and isoheptane selectivity of 86%, respectively, compared with other catalysts in the same system. The study also provides new ideas for the preparation of molecular sieve materials.

Keywords Ni/SAPO-11 · Instant exactness synthesis (IES) method · Hydroisomerization · N-heptane

1 Introduction

Since the discovery of the fossil fuel, humans have become hugely dependent on it to maintain the functioning of the modern society. However, the combustion of gasoline leads to the emission of harmful gases into the atmosphere, causing the greenhouse effect. Octane number is an indicator used to judge the resistance of gasoline explosion performance. N-heptane which is an usual component in gasoline is extremely easy to cause the explosion, so its octane number is set to zero. Increasing the octane number of gasoline has been proved to be extremely challenging, because it is an important component of aviation fuel. Some researchers have removed oxygen from biodiesel (FAME) by hydrodeoxygenation (HDO), decarbonylation and decarboxylation [1, 2]. However, the existence of n-heptane with the characteristics of high pour point and high cloud point reduces the performance of gasoline [3]. Some strategies [4] indicate that the process of hydroisomerization can eliminate n-alkanes and other by-products. For petrochemical industry, it is of great significance to obtain high octane gasoline by hydroisomerization of light alkanes [5–7]. According to the report, a high-quality lubricant base oil with a high viscosity index and a low freezing point can be obtained by catalytic dewaxing process [8].

Since the aluminophosphate molecular sieves were invented in 1982 [9], this kind of zeolitic materials which

---

Wei Zhang and Yanhua Suo are the co-corresponding authors for this article

Electronic supplementary material The online version of this article (https://doi.org/10.1007/s10934-020-00920-1) contains supplementary material, which is available to authorized users.

✉ Wei Zhang
99095871@qq.com

✉ Yanhua Suo
33367123@qq.com

[1] College of Chemistry and Chemical Engineering, Northeast Petroleum University, 99# Xuefu Street, High-tech Industrial Development District, Daqing 163318, Heilongjiang, People's Republic of China

[2] Daqing Science and Technology Bureau, Daqing 163000, People's Republic of China

were consisted of corner-sharing O vertices among neighbouring tetrahedral TO_4 (T = Si, Al, P, etc.) [10, 11] with rich structural diversity had been widely devoted to the field of separation [12, 13], ion-exchangers, gas adsorption [14, 15], acid catalysts [16], and catalyst supports [17] et al. Thus, a catalyst with an appropriate pore topology and an excellent balance between acid sites and metal sites seems to play an important part in the process. Just as some studies have revealed, the mesostructure, porosity and pore size distribution would affect the performance of catalyst [18, 19]. The distinguished catalytic performance [20–23] is related to silicoaluminophosphate (SAPO) which has straightforward AEL structure and 10-membered ring channels with diameters of 0.39 nm × 0.63 nm and the bridging OH relevant with Si–O–Al bonds. Not only the acidity of SAPO-11 affects the catalytic performance directly, but also the structure of the crystal states the product distribution [24, 25]. For the recent status, some researchers reported that precious metals (Pt, Pb) are commonly used to prepare bifunctional catalysts, which exhibited excellent catalytic performance. However, during the preparation of precious metal catalysts, the continuous addition of chlorine inevitably causes environmental pollution [26], and its high cost makes it difficult to advance in the process of industrialization. The experiment carried out by Liu et al. [27] suggested that Ni/SAPO-11 catalyst had a good effect on processes of deoxygenation and hydroisomerization, which gave a high liquid alkane yield of 70 wt%. It is known that the hydroisomerization of n-alkanes is realized by (de)hydrogenation processes on metallic sites and skeletal rearrangement [28]. Many reports had focused on the development strategy of non-precious metals represented by nickel metal [29, 30].

Hydrothermal synthesis is a traditional method to prepare molecular sieves, while this method is no longer satisfactory because of its many disadvantages. Due to the self-polymerization of crystal nuclei, the molecular sieve produced by this method exhibited cracked pseudo-spherical aggregates in the range of 3 to 10 μm [31]. It is reported that conversion of isomerization of n-heptane could be over 75.7% by using the Ni/SAPO-11 catalyst prepared by two-step hydrothermal crystallization method [32]. However, the two-step hydrothermal crystallization method would result in the increase of uncontrollable factors generated during the complex preparation process, which may finally reduce the performance of the catalyst. Zhang et al. [33] had reported a stable SAPO-11 molecular sieve with nanosheet morphology. The nanosheet-like SAPO-11 molecular sieve could maintain suitable acidity by partially blocking some acidic sites, which led to a higher isomer selectivity of 90% in the hydroisomerization of n-dodecane. But the nanosheets are easy to decompose under high-temperature conditions. Obviously, all of these disadvantages affect the performance of the catalyst for hydroisomerization, and it is significantly important to find an effective and innovative preparation strategy.

As far as we know, Ni/SAPO-11 catalysts with high-performance of n-heptane isomerization have not been reported. The Instant Exactness Synthesis (IES) method, inspired by traditional hydrothermal synthesis, was proposed in our recent work. Comparing with the hydrothermal synthesis method, the main advantages of the IES are: (i) It has faster crystal growth rate and it can facilitate the formation of hierarchical micro-, meso-, and macrostructures, so that it will benefit the mass transfer in the reactions; (ii) It owns controllable crystal morphology and chemical composition; (iii) It can reduce the consumption of organic materials and the discharge of polluted water. In order to fully demonstrate the superior performance of the IES method, it was compared with the traditional hydrothermal synthesis method. Besides, the growth mechanism was elaborated from the perspective of crystal growth kinetics, and the mechanism of isomerization reaction was also described from the theory. Benefiting from the IES method, Ni/SAPO-11-IES catalyst with n-heptane conversion of 82% and isoheptane selectivity of 86% was obtained. The result of n-heptane hydroisomerization is identified as a pioneer in the same system reported, which demonstrates the IES method has a broad application prospect. At the same time, this new method provides a new strategy for the preparation of molecular sieves of SAPO series.

2 Experimental

2.1 Chemical reagents

Pseudo-boehmite (70.0 wt% Al_2O_3, Dezhou Jinghuo Technology Glass Co., Ltd., China), TEOS (Damao, 28.0 wt% SiO_2), H_3PO_4 (Aladdin, ≥ 85 wt%), Dipropylamine (DPA, Aladdin, 99.0 wt%), Nickel nitrate [Damao, $Ni(NO_3)_2 \cdot 6H_2O \geq 85.0$ wt%].

2.2 Preparation of SAPO-11-IES

SAPO-11-IES was synthesized by the IES method following the procedure in Fig. S1. The pseudo-boehmite, phosphoric acid, colloidal silica and di-propylamine (DPA) were mixed together with the molar composition of 1.0 P_2O_5: 1.0 Al_2O_3: 0.4 SiO_2: 1.0 DPA. After stirring for about 5–10 min, the amorphous mixture was obtained, which was viscous with wrapping the water from the raw material (eg: physically adsorbed water on pseudo-boehmite, H_3PO_4 solution, and TEOS). The amorphous mixture was transferred into an autoclave and subjected to crystallization (200 °C, 24 h). The final product was washed with deionized water and activated at 600 °C for 4 h, and named as SAPO-11-IES. Preparation of SAPO-11-H.

In a typical synthesis, the chemical composition of the amorphous mixture was 1.0 P_2O_5: 1.0 Al_2O_3: 0.4 SiO_2: 1.0 DPA. Pseudo-boehmite, phosphoric acid, and TEOS were used as aluminum, phosphorus, and silicon sources, respectively. Pseudo-boehmite was dissolved in deionized water, and then phosphoric acid was added dropwise. When the above mixture became homogeneous, di-n-propylamine (DPA) was added to the mixture under continuous stirring. Then TEOS was slowly added to the above mixture with continuous stirring. Finally, the resulting hydrogel was transferred into autoclave and subjected to crystallization (200 °C, 24 h). The final product was washed by deionized water and activated at 600 °C for 4 h, and named as SAPO-11-H.

2.3 Preparation of catalysts

Bifunctional catalysts were synthesized by the impregnation method with aqueous $Ni(NO_3)_2{\cdot}6H_2O$. A certain amount of concentrated $Ni(NO_3)_2{\cdot}6H_2O$ solution was added to 1.0 g of SAPO-11 sample, and the loaded amount of Ni was 4 wt%. The sample was left at room temperature for 24 h and dried at 80 °C overnight. After that, the sample was calcined in air at 480 °C for 4 h. The bifunctional catalysts, which were prepared from SAPO-11-H and SAPO-11-IES samples separately, were named as Ni/SAPO-11-H and Ni/SAPO-11-IES, respectively.

2.4 Characterization

Powder X-ray diffraction patterns (XRD) analysis was carried out on the diffractometer (D/Max 2200 PC, Rigaku Corp., Japan) with Cu Kα radiation (1.514 Å) and the scan rate is 5°/min operated at 40 kV and 40 mA. N_2 adsorption–desorption measurements were carried out with an ASAP 2020 Micromeritics instrument. The specific surface area was obtained by Brunauer Emmet Teller (BET) analysis. The scanning electron microscope (SEM) was employed on FEI Verios 460. NH_3-TPD and H_2-TPR were obtained on AutoChem1 2920. Also, in order to research the lattice of SAPO-11, Transmission Electron Microscopy (TEM) analysis was performed using FEI Talos F200s at an acceleration voltage of 200 kV. X-ray photoelectron spectroscopy (XPS) was carried out by the Thermo Fisher Escalab 250XI apparatus. ^{29}Si MAS NMR was carried out by JNM-ECZ600R. UV–vis–DRS was recorded with Shimadzu UV3600. Differential scanning calorimetry/thermogravimetric analysis (DSC/TGA) data was obtained by the NETZSCH STA449C/6/G apparatus. X-ray Fluorescence Spectrometer (XRF) was obtained on Panalytical Axios. And FT-IR was carried out on Bruker Equinox 55.

2.5 Catalytic testing

The hydroisomerization reaction of n-heptane (n-C_7) was conducted in a continuous flow fixed-bed reactor loaded with 1.0 g catalyst. A schematic diagram for the process of n-heptane hydroisomerization on a fixed bed is shown in Fig. S2. The reaction was conducted under constant pressure with n(H_2)/n(n-C_7) of 14, WHSV of 6.8 h^{-1} and reaction temperature of 250–350 °C. Before the reaction, the catalysts were reduced in a hydrogen stream at 400 °C for 4 h. Then, the temperature was lowered to 350 °C and n-C_7 was pumped to the reactor.

3 Results and discussion

3.1 XRD characterization

Figure 1a shows the XRD patterns of SAPO-11-H and SAPO-11-IES samples. The figure shows a series of sharp and strong diffraction pattern, indicating the samples behave excellently in crystallinity. There were no peaks of impurities, indicating both of the samples exhibited well-crystalline framework structure of AEL type [24, 34]. The structure of SAPO-11 (AEL type) series molecular sieves [35] was similar to SAPO-31 (ATO type) and no phase transformation was

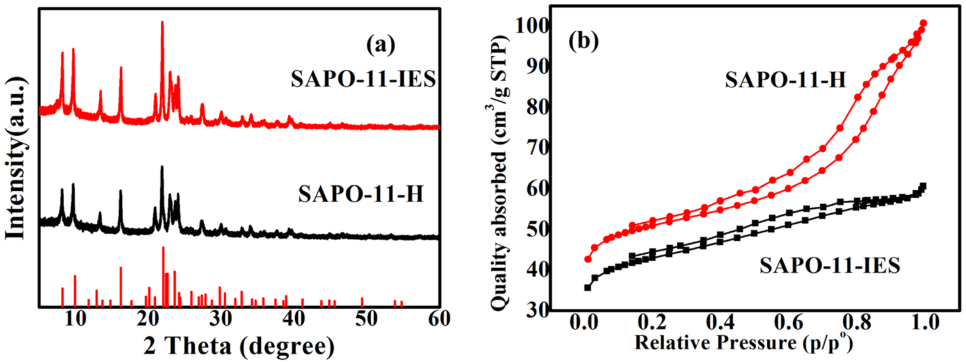

Fig. 1 **a** XRD patterns of SAPO-11-IES and SAPO-11-H. Red vertical lines represent the standard XRD pattern card of SAPO-11. **b** Nitrogen adsorption and desorption isotherms of SAPO-11-IES and SAPO-11-H samples

observed in our work, and it meant that the grinding process could meet the synthesis conditions accurately. Compared with SAPO-11-H, the peak width of SAPO-11-IES narrowed a little, which may be caused by the difference of grain size. Another point that should not be ignored was that the peak of SAPO-11-IES sample was much stronger than SAPO-11-H, which meant the sample prepared by the grinding process performed better crystallinity than the traditional hydrothermal method. Moreover, the increased crystallinity of the SAPO-11-IES during the grinding process may imply the compounds in the synthetic gels played a considerable role in the growth of crystallization.

3.2 N_2 Adsorption–desorption characterization

Figure 1b displays the nitrogen adsorption and desorption isotherms of SAPO-11-IES and SAPO-11-H, respectively, which showed type I and type II isotherms with hysteresis loops. Both the samples had shown the characteristics of microporous structure [25]. The similarity of the micropore volume of the two samples (Table 1) proved that the grinding process did not lead to significant transformation. For further steps, the BET surface area (Table 1) of SAPO-11-IES (152 m^2/g) was larger than that of SAPO-11-H (135 m^2/g), and it can be explained by the filling of the micropores of SAPO-11-IES. The isotherm loops which were caused by the multilayer adsorption on the sample can be observed when $p/p_0 > 0.1$, and this phenomenon confirmed the existence of mesopores and macropores [36].

3.3 SEM characterization

Figure 2a and c demonstrate the SEM images of the whole view, and Fig. 2b and d display the individual particles of SAPO-11-H and SAPO-11-IES, respectively. Irregular spherical particles or circular aggregates can be observed from both of the samples. Describing in details, SAPO-11-IES sample behaved relatively regular circular aggregates and compact surface, while the SAPO-11-H sample exhibited different sizes of spherical aggregates (1.8–4.3 μm). It is especially noteworthy that SAPO-11-H sample was consisted of fine particles, which corresponded to the large hysteresis loops when $p/p_0 > 0.36$ observed in the characterization of nitrogen adsorption and desorption shown in Fig. 1b.

3.4 NH_3-TPD characterization

NH_3-TPD measurement was used to compare the acidity of SAPO-11-IES and SAPO-11-H. As depicted in Fig. 3a,

Table 1 Textural properties of synthesized SAPO-11-IES and SAPO-11-H samples

Sample	S_{BET} (m^2/g)	S_{micro} (m^2/g)	S_{Ext} (m^2/g)	V_{total} (cm^3/g)	V_{micro} (cm^3/g)	Average pore width (Å)
SAPO-11-IES	152	109	43	0.153	0.051	39.9
SAPO-11-H	135	94	40	0.094	0.043	27.7

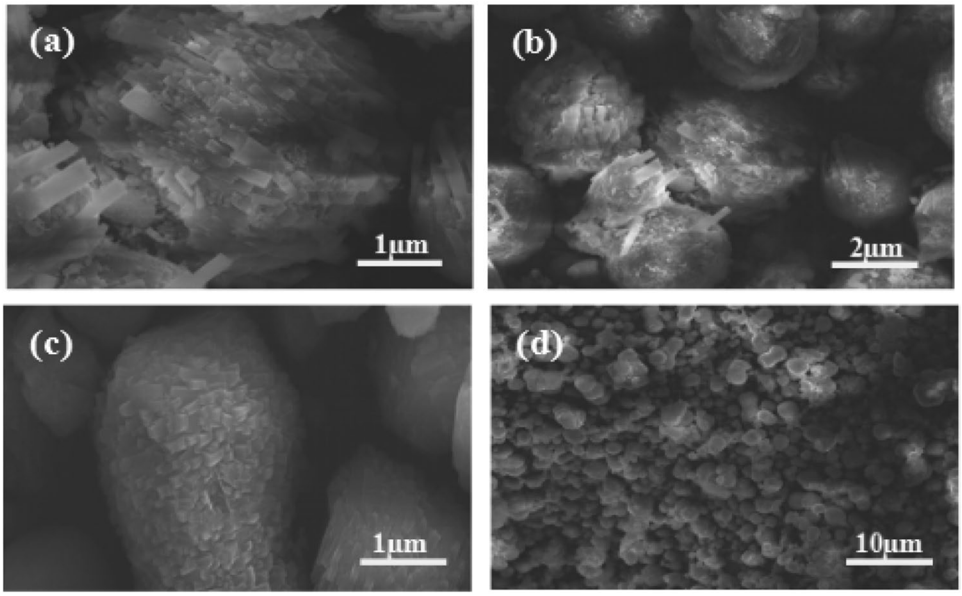

Fig. 2 SEM images of SAPO-11-H (**a** and **b**), and SAPO-11-IES (**c** and **d**)

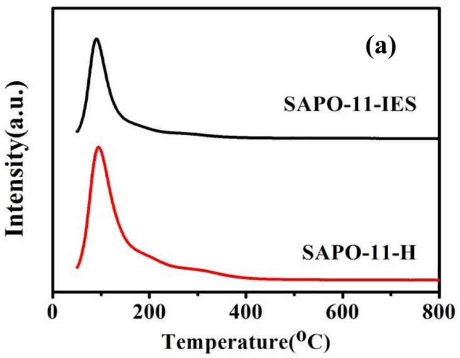

Fig. 3 **a** NH_3-TPD profiles of SAPO-11-IES and SAPO-11-H samples. **b** H_2-TPR profiles of samples Ni/SAPO-11-H and Ni/SAPO-11-IES

two distinct desorption peaks could be observed at 92 °C and 311 °C, which were caused by P-OH (representative of weak acid center) and bridged hydroxyl (representative of medium-strong acid center). Between 49 and 258 °C, the desorption peaks corresponded to the desorption of NH_3 adsorbed on the weak acid center of the SAPO-11 skeleton. While between 286 and 403 °C, the image reflected medium and strong acidity center on SAPO-11 skeleton. According to the above characterization, it could be concluded that SAPO-11-IES had a relatively higher medium and strong acidity when compared with SAPO-11-H. Therefore, SAPO-11 prepared by IES method could provide suitable acid sites, and it can be inferred that there will be more appropriate active sites for hydroisomerization. The active sites could create a situation for the unsaturated nickel cations to produce Lewis acid sites and compensate the acid loss [37].

3.5 H_2-TPR characterization

In order to illustrate the reduction ability of the catalyst, H_2-TPR measurement was carried out. Figure 3b shows the H_2-TPR profiles of the samples. It could be observed two clear and distinct H_2 reduction peaks from the overall curve in the range of 100 and 700 °C, which were caused by different nickel species interacting weakly and strongly with the support, respectively. These two different peaks corresponded to strong and weak interaction of nickel species with the carriers in the main channels and hidden sites [38]. It is ascribed to the reduction of bulk NiO species for the appearance of the first peak (359 °C for Ni/SAPO-11-IES and 343 °C for Ni/SAPO-11-H). As for the second peak (465 °C for Ni/SAPO-11-IES and 434 °C for Ni/SAPO-11-H), it is attributed to the reduction of nickel oxide, which behaved strong interaction with the carrier. According to the report [8], the stronger the interaction behaves, the higher the Ni dispersion will be. Therefore, it could be inferred that Ni/SAPO-11-IES exhibited a higher dispersion than that of Ni/SAPO-11-H, for the Ni species of Ni/SAPO-11-IES behaved a relatively strong interaction with the SAPO-11 support.

3.6 TEM characterization

In order to further illustrate the catalytic performance of Ni/SAPO-11-IES in Fig. 4a, c and Ni/SAPO-11-H in Fig. 4b, d, the TEM and HRTEM images, EDS energy spectrum (Fig. S3) and elemental mapping (Fig. S4) of the samples were carried out. It could be seen from the EDS energy spectrum that both the samples exhibited a similar Ni loading. The particle size distribution of the two samples were shown in Fig. 4a and b, from which the particle size could be confirmed. Obviously, the particle size of Ni/SAPO-11-IES was about 1.8–4.6 nm, and the particle size of Ni/SAPO-11-H was about 2.3–7.1 nm. Figure 4c and d exhibited the HRTEM images of SAPO-11-IES and SAPO-11-H, respectively. The interplanar distances were 0.21186 Å for SAPO-11-IES and 0.2475 Å for SAPO-11-H calculated from the HRTEM images. Smaller interplanar spacing meant that SAPO-11-IES exhibited higher crystallinity, which was also consistent with the XRD results. Elemental mapping (Fig. S3) was employed to demonstrate the existence of Ni, P, Al, Si elements, which reflected the uniform distribution of the loaded Ni, and it was in accordance with the catalyst performance evaluation in the following discussion.

3.7 XPS analysis

The X-ray photoelectron spectra shown in Fig. 5 was applied to elucidate the Ni element valence state and nature of nickel species. Both the catalysts of Ni/SAPO-11-H (Fig. 5a) and Ni/SAPO-11-IES (Fig. 5b) displayed the main peaks $2P_{3/2}$ and $2P_{1/2}$, and the corresponding satellite peaks were vividly depicted in the figure above. For Ni/SAPO-11-H, the peak at 861.1 eV contributed to the existence of nickel species, while the peak at 879.5 eV was caused by the interaction between NiO and SAPO-11-H molecular sieve [39, 40]. To further support our opinion, the deconvolution technique for the samples were performed, and a simplified model of final-state effects could account for the appearance of main peaks at Ni $2P_{3/2}$, and photoemission may be accompanied by rearrangement of electrons in the valence band [30, 41].

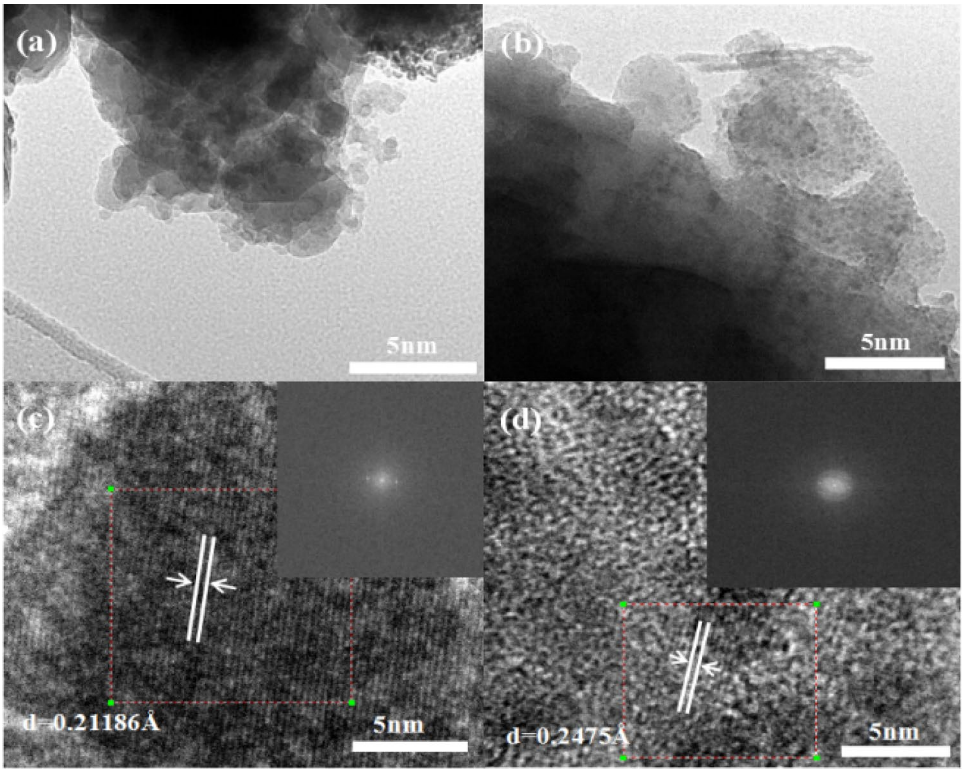

Fig. 4 TEM images of Ni/SAPO-11-IES (**a**, **c**) and Ni/SAPO-11-H (**b**, **d**) catalysts

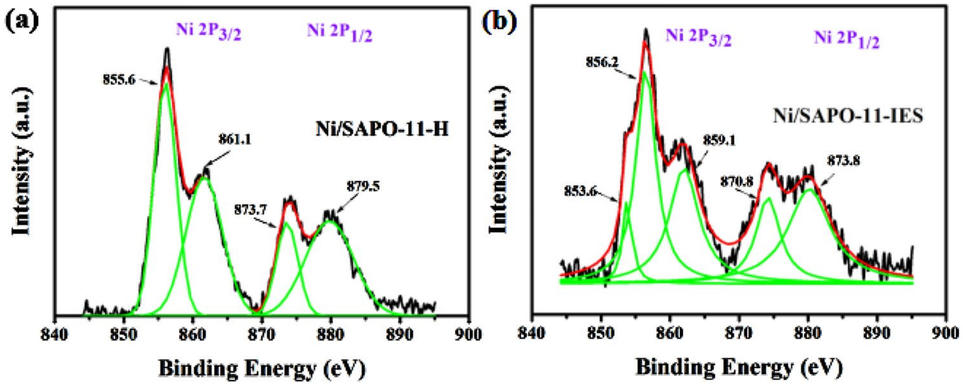

Fig. 5 XPS spectra of the Ni 2p core level for calcined Ni/SAPO-11-H, Ni/SAPO-11-IES samples recorded at room temperature

For SAPO-11-IES, the peak at 856.2 eV of Ni $2P_{3/2}$ and the peak at 873.8 eV of Ni $2P_{1/2}$ were mainly comprised by the octahedral Ni^{2+} (provided by NiO), which reacted with SAPO-11-IES violently [42, 43].

3.8 UV–vis diffuse reflectance characterization

UV–vis diffuse reflectance spectra are shown in Fig. 6. UV–vis spectrum of Ni/SAPO-11-H catalyst was similar to that of bulk NiO according to the reported literature [30]. The catalyst exhibited the absorption bands at 280, 375, 403, 640 and 720 nm. This phenomenon demonstrated that the existing state of nickel species in Ni/SAPO-11-H was NiO [44]. Furthermore, this result implied that nickel ions do not participate in the zeolitic framework. A piece of evidence that could support this view was that, once the heteroatoms were incorporated into the framework, the framework distortion of molecular sieves would be observed obviously [45–48]. Since the existence of silicon atoms inhibited the isomorphous substitution of nickel ions, the stability of the molecular sieve skeleton could be guaranteed. For Ni/SAPO-11-IES, the absorption bands at 263 nm may be due to the transfer of an electron from O^{2-} to Ni^{2+}.

3.9 ^{29}Si MAS NMR characterization

^{29}Si MAS-NMR spectra of SAPO-11-H and SAPO-11-IES are revealed in Fig. 7a and b. Above all, both the samples

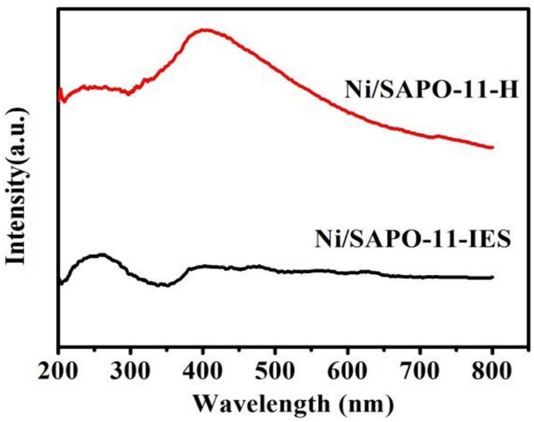

Fig. 6 UV–vis diffuse reflectance spectra of the calcined Ni/SAPO-11-H and Ni/SAPO-11-IES

synthesized by different methods covered a wide range of spectra from − 40 to − 140 ppm, which implied that various frameworks of Si species existed in the samples and a large amount of multiple Si environments appeared in the molecular sieve [34]. In addition, the central peaks of the ^{29}Si MAS-NMR spectra of SAPO-11-H and SAPO-11-IES were at 77 ppm and 83 ppm, respectively. Obviously, there was about 6 ppm shift to the higher chemical shift, which may be caused by the reduction of Si islands formed in SAPO-11-IES sample. The deconvolution process was carried out to confirm the type of Si, the resonance peaks of which situated at about − 92, − 83, − 80, − 76, and − 72 ppm, respectively. The silicon types corresponding to these peak positions were Si (4Si), Si (1Al,3Si), Si (2Al,2Si), Si (3Al,1Si), and Si (4Al), respectively. By employing ^{29}Si MAS-NMR characterization technique, Si species of type 4Al was confirmed in silicoaluminophosphate region, while on the other hand, Si species of type nAl and 4-nSi remained on the edges of non-acidic silica islands. Generally, rearrangement of active components existed in the crystallization process of molecular sieves [49, 50]. By comparing the SAPO-11-IES sample obtained by the IES method with the SAPO-11-H sample synthesized by the hydrothermal method, it could be concluded that the sample prepared by the IES method possessed more Si species. And XRF (Table S1) was carried out to further confirm that the sample synthesized by the IES method showed a higher silicon content. Combining ^{29}Si MAS-NMR with NH_3-TPD (Fig. 3a) measurement, it could be found that the reason for the higher medium and strong acidity of SAPO-11-IES could be ascribed that there were more Si species and Brønsted acid sites existed in SAPO-11-IES. This kind of SAPO-11 catalyst with suitable acid sites and high dispersion degree was considered to be particularly suitable for hydroisomerization of long-chain alkanes.

3.10 TG-DSC characterization

In order to exclude the influence of the transformation of the crystal structure at a higher temperature on the isomerization effect of the catalyst, the TG-DSC measurement (Fig. 8) was employed. In the range of 50–200 °C, dramatic physical and chemical changes had performed. Subtle change of TG curve corresponded to the DSC curve could be observed at about 88.3 °C for SAPO-11-IES and 72.5 °C for SAPO-11-H, respectively, and the endothermic peak could be observed to appear simultaneously. Obviously, sublimation starting temperature of SAPO-11-IES was higher than that of SAPO-11-H, indicating that the SAPO-11 support materials prepared by IES method were more stable. Both the weight loss on the TG curve and the escape of volatile corresponded to the peaks on DSC curves. It could be observed that the energy changes drastically while the weight changes less, which indicated that both of the synthesized samples exhibited a stable crystal structure [51]. The residue was deemed to be the product of some impurities of the molecular sieve after the weight loss. The stability of materials provided safeguards for the following superior isomerization effect.

Fig. 7 Si^{29} MAS-NMR spectra of the SAPO-11-H (**a**) and SAPO-11-IES) (**b**) samples. Black and red curves correspond to the experimental and simulated data, respectively

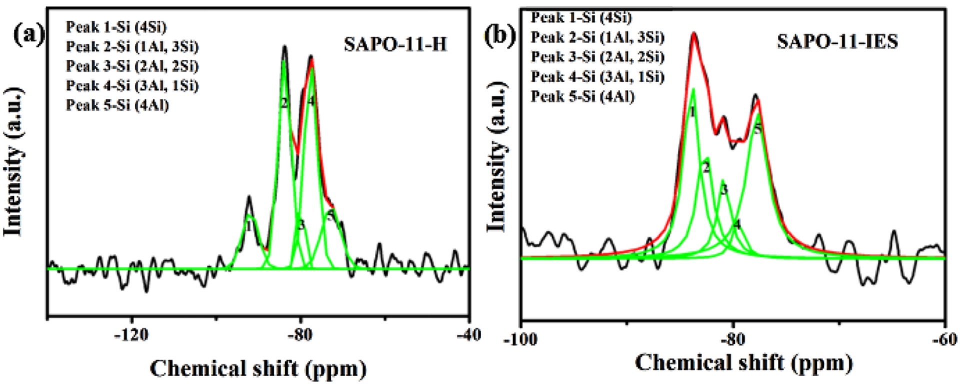

Fig. 8 TG-DSC curves of SAPO-11-H (**a**) and SAPO-11-IES (**b**) samples

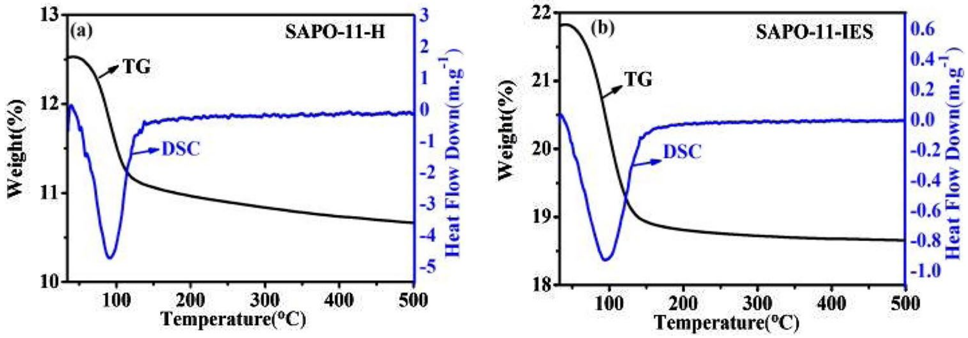

3.11 Growth mechanism

In order to illustrate the growth process of the molecular sieve more clearly, the corresponding growth mechanism was further elaborated. In the mixture gel, pseudo-boehmite was transformed into tetra-coordinated aluminum species due to the IES method, and the interactions between tetra-coordinated aluminum and DPA molecules contributed to the formation of penta-coordinate aluminum [52]. Also, the IES method enhanced the interactions between tetra-coordinated aluminum and water, which promoted hexa-coordinated aluminum. Thus, it could be deduced that IES method could accelerate the formation of highly condensed polyphosphate species from the depolymerization of condensed species to oligomeric states. At the moment of the formation of highly condensed polyphosphate species, the Al–O–P units were absence, but Al and P units would form multiple rings and branched ring units when the reaction time and reaction temperature was sufficient in the intermediates [53]. As was reported [54], the concentration of long-range ordering layered phase would increase during the transformation from amorphous phosphorus to tetra-coordinated phosphorus. IES method promoted the transformation from condensed polyphosphates to short-chain polyphosphates [24], which played a key role in the construction of framework structures. XRD results of SAPO-11-IES and SAPO-11-H (Fig. S6) confirmed the best crystallization time. By comparing the images, it could be found that when the crystallization time was 0.5 h and 1 h, the SAPO-11 sample cannot be obtained. And it could be also found that the samples crystallized better with the prolong of the crystallization time when it was more than 1.5 h, while the sample prepared by IES method could maintain a superior state until the crystallization time was 24 h, indicating that 24 h was the best crystallization time.

4 Catalytic performance of n-heptane hydroisomerization

It can be known from the above characterization results that SAPO-11-IES exhibited ultra high crystallinity, regular spherical particles, dense surface, high stability, and high dispersion. These excellent characteristics guaranteed that SAPO-11-IES could be a superior catalyst for the isomerization reaction. The catalytic performances of SAPO-11-IES, SAPO-11-H, Ni/SAPO-11-IES and Ni/SAPO-11-H for n-heptane hydroisomerization were shown in Fig. 9, and SEM images of samples Ni/SAPO-11-IES and Ni/SAPO-11-H were shown in Fig. S5. Hydroisomerization of n-heptane was carried out under the temperature range from 260 to 340 °C on all of the synthesized Ni/SAPO-11-IES, Ni/SAPO-11-H, SAPO-11-IES, and SAPO-11-H catalysts. It could be observed that the conversion of n-heptane reached

Fig. 9 Conversion of n-heptane versus temperature (**a**) and selectivity to isomers versus conversion (**b**) over Ni/SAPO-11-H and Ni/SAPO-11-IES catalysts

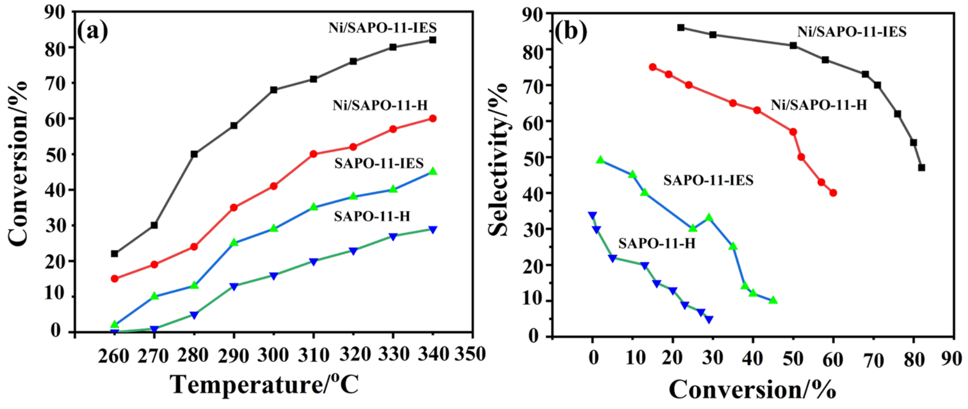

82%, and the selectivity of isoheptane reached 86% for Ni/SAPO-11-IES when the reaction temperature was 340 °C, while the conversion of n-heptane was only 60%, and the selectivity of isoheptane was only 75% for Ni/SAPO-11-H when it was at the same reaction temperature. While for catalysts SAPO-11-IES and SAPO-11-H which had not been modified with metallic Ni, the conversion of n-heptane was 45%, and the selectivity of isoheptane was 49% for SAPO-11-IES when the reaction temperature was 340 °C, and the conversion of n-heptane was only 29%, and the selectivity of isoheptane was only 34% for SAPO-11-H, when it was at the same reaction temperature. After discussing the conversion and selectivity of the catalyst before and after loading metal Ni, it could be found that the performances of the catalysts modified with Ni were about doubled compared with the catalysts without Ni modification. The huge improvement in catalytic performances of catalysts modified with Ni meant there were more active sites in the catalysts modified with Ni. And it could also prove that metallic Ni was a key active site for (de)hydrogenation in the catalytic hydroisomerization reaction of n-heptane to enhance the conversion as well as the selectivity [55]. Nevertheless, it can be found that the catalysts SAPO-11-IES and SAPO-11-H which had no active site of metal also exhibited an selectivity for isoheptane to some extent, and this is not consistent with the mechanism of the bifunctional catalyst for n-heptane isomerization as it reported before [56, 57]. Therefore, it can be deduced that the catalytic mechanism of bifunctional catalyst should be supplemented further by other mechanisms to explain the phenomenon of the catalyst behaved here for n-heptane isomerization, and it would be studied further in detail in future. As the temperature rose, the conversion of n-heptane and cracking of the carbon chain became extremely violent, while the isomer selectivity tended to significantly weaken. Another point that should not be ignored was that Ni/SAPO-11-IES performed higher selectivity for isomers and lower selectivity for cracking products than that of Ni/SAPO-11-H.

The superior catalytic performance of Ni/SAPO-11-IES could be ascribed to the relatively more Brønsted acid sites with the medium and strong acidity [58, 59], which had demonstrated by the above measurements of NH_3-TPD and ^{29}Si MAS already. The Brønsted acid sites could be obtained more easily from the stable nanocrystalline of Ni/SAPO-11-IES compared with Ni/SAPO-11-H. Besides, there were more available pores in SAPO-11-IES and Si species in SAPO-11-IES sample obtained from the BET and ^{29}Si MAS NMR characterizations, which also made it possible to be a superior candidate for n-heptane hydroisomerization. Furthermore, the high conversion of n-heptane and high selectivity could be attributed to the appropriate balance between the metal and acid sites existing in the SAPO-11 catalysts synthesized by IES method. In fact, both the suitable ratio of medium strong acid sites and metal sites could facilitate the isomerization reaction [56, 57]. And only if the amount of metal ions was sufficient for the hydrogenation or dehydrogenation process, the acid sites of the molecular sieves could determine the catalytic activity of isomerization. The five different silicon environments shown in the ^{29}Si MAS NMR corresponded to the strong acid centers in NH_3-TPD characterization, and EDS images and elements mapping demonstrated the outstanding dispersibility of nickel metal, which provided the suitable metal sites for Ni/SAPO-11 catalyst. Therefore, it could be concluded that the suitable ratio of medium strong acid sites and metal sites, both of which could be obtained form the Ni/SAPO-11-IES sample, and both of the strong acid sites and metal sites were sufficient in Ni/SAPO-11-IES. In addition, the existence of multiple Si substances made SAPO-11-IES rich in medium and strong acid centers, which increased the activity of its catalyst. What's more, the results of Wang et al. also confirmed the important role of acid sites in the catalytic reaction [60]. Yang et al. also revealed that the spatial distribution of single Ni sites on the support had an impact on the catalytic performance, and higher dispersion could provide a higher catalytic performance. The result of our work behaved much better than those reported in the previous work, which is displayed in Table S2.

The reaction mechanism of isomerization reactions were just as Eqs. 1–5 shown below:

$$n - C_7H_{16} \Leftrightarrow n - C_7H_{14} + H_2(\text{Metal Center}) \tag{1}$$

$$n - C_7H_{14} + H^+ \Leftrightarrow n - C_7H^+_{15}(\text{Acid Center}) \tag{2}$$

$$n - C_7H^+_{15} \Leftrightarrow i - C_7H^+_{15}(\text{Acid Center}) \tag{3}$$

$$i - C_7H^+_{15} \Leftrightarrow i - C_7H_{14} + H^+(\text{Acid Center}) \tag{4}$$

$$i - C_7H^+_{14} + H_2 \Leftrightarrow i - C_7H_{16}(\text{Metal Center}) \tag{5}$$

The isomerization reaction of n-heptane on a bifunctional catalyst followed carbenium ion mechanism [61, 62]. The process of hydroisomerization of heptane was vividly demonstrated in Fig. 10. The n-heptane molecules dehydrogenated on nickel sites, and the rearrangement of acidic sites were realized by carbenium ion formed after protonation of the intermediate. The n-heptane isomers was generated by hydrogenation of the rearranged intermediates on nickel active sites. The cleavage reaction was considered to be the primary side reaction. Above all, the metallic nickel was the active site for (de)hydrogenation, and the acidic sites were the active sites for the isomerization. Then it can be concluded that the surface enriched by Ni and porous support played a vital role in the catalyst activity [55].

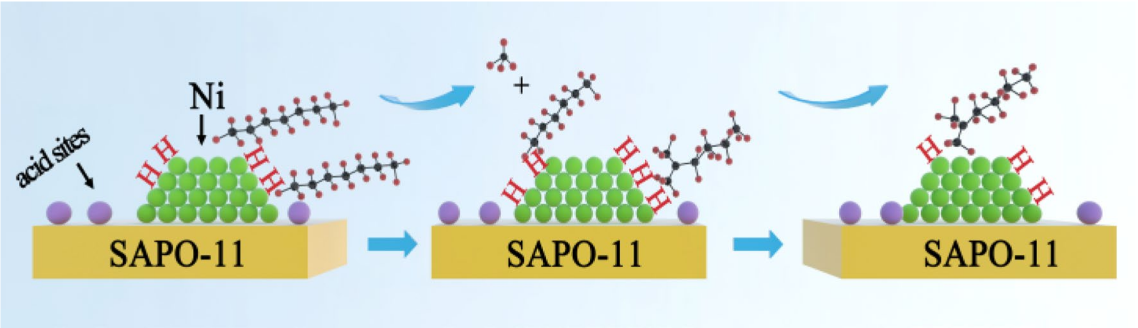

Fig. 10 Schematic diagram of hydrogen isomerization process of heptane

The superior catalyst performance is explained more precisely in terms of the diffusion of SAPO-11 and the kinetics on product distribution. In order to study the effect of pore structure of SAPO-11 on the diffusion of heptane molecules, Fick's second law is used to illustrate the molecular concentration in the channel as a function of time [24]:

$$\frac{\partial C}{\partial t} = D\left(\frac{\partial^2 C}{\partial x^2}\right) \tag{6}$$

where C is the concentration of n-heptane inside the particle, t is time, D is the effective diffusivity, and x is the diffusion length. For the hydroisomerization of n-heptane, the isomer selectivity of the catalyst was a function of temperature. The impact of acid site density and strength was almost negligible for the kinetic influences of relevant acid sites. Therefore, the influence in activity and selectivity and the diffusion properties dominated by pore structure can be assigned to a function. When the diffusion restriction mechanism does not occur, the overall activation energy is:

$$E_1 = RT^2 \frac{\partial \ln(r)}{\partial T} = \Delta E_2 \tag{7}$$

It can be learned that smaller crystallite size of Ni/SAPO-11-IES catalyst improved the isomer selectivity, which may be caused by faster diffusion rates of isomers in the micropores. When the reaction performed the diffusion control, the diffusion of isomers would play a decisive role in the reaction rate. The Arrhenius equation can represent the functional relationship between them:

$$k = k_0 e \frac{-\Delta E_2}{RT} \tag{8}$$

$$D = D_0 e \frac{-\Delta E_3}{RT} \tag{9}$$

where k is the rate constant, and D is the diffusion constant. At this moment, the kinetics of the reaction proceeded toward the direction of the cleavage reaction. The larger crystallite size and longer diffusion path of Ni/SAPO-11-H would lead to long residence time of the branch of alkane, and thus Ni/SAPO-11-H was prone to proceeding toward the direction of the cleavage reaction. While Ni/SAPO-11-IES catalyst was equipped with smaller crystallite size and more reasonable pore structure, and this structure characteristic would create a shorter residence time [63]. Thus the occurrence of cleavage reactions could be greatly reduced. After hydrogenation, the higher the degree of skeletal isomerization, the larger the volume of molecules involved in the reaction, and this would influence the diffusion behavior of the product molecule to a certain extent, which finally influenced the catalytic performance of the catalyst.

5 Conclusions

In this research, the new IES method was used to prepare Ni/SAPO-11 catalyst with high catalytic performance of n-heptane isomerization. By carrying out a series of characterizations, it can be concluded that a catalyst with high crystallinity, high specific surface area, regular circular aggregates and compact surface was obtained. The extraordinary catalytic activity of isomerization is determined by the sufficient acid sites provided by Si species and metal sites provided by highly dispersed metallic Ni particles of the molecular sieves. The catalytic mechanism and growth mechanism were elaborated in detail from the perspective of kinetics and crystal growth process. Finally, n-heptane hydroisomerization of Ni/SAPO-11 catalysts were conducted as a probe, and exhibited the higher conversion rate of 82% and isoheptane selectivity of 86% for Ni/SAPO-11-IES compared with that of Ni/SAPO-11-H. These findings will provide a new strategy for the fabrication of catalysts and could further strengthen the competitiveness in the field of catalysis.

Acknowledgements This study was supported by the Cultivation Fund of Northeast Petroleum University [Grant No. 2017PYYL-03].

Compliance with ethical standards

Conflict of interest There are no conflicts to declare.

References

1. B. Donnis, R.G. Egeberg, P. Blom, K.G. Knudsen, Top. Catal. **52**(3), 229 (2009)
2. G.W. Huber, P. O'Connor, A. Corma, Appl. Catal. A. **329**, 120 (2007)
3. S. Zhao, M.F. Li, Y. Chu, J.X. Chen, Energy Fuels. **28**, 7122 (2014)
4. T.M. Kalnes, K.P. Koers, T. Marker, D.R. Shonnard, Environ. Prog. Sustain. **28**(1), 11 (2009)
5. J. Pastvova, D. Kaucky, J. Moravkova, J. Rathousky, S. Sklenak, M. Vorokhta, L. Brabec, R. Pilar, I. Jakubec, E. Tabor, P. Klein, P. Sazama, ACS Catal. **7**, 5781 (2017)
6. K. An, S. Alayoglu, N. Musselwhite, K. Na, G.A. Somorjai, J. Am. Chem. Soc. **136**, 6830 (2014)
7. V.M. Akhmedov, S.H. Al-Khowaiter, Catal. Rev. **49**, 33 (2007)
8. Y.Y. Du, B. Feng, Y. Jiang, L. Yuan, K.K. Huang, J.S. Li, Eur. J. Inorg. Chem. **22**, 2599 (2018)
9. S.T. Wilson, B.M.C. Lok, A. Messina, T.R. Cannan, E.M. Flanigen, J. Am. Chem. Soc. **104**, 1146 (1982)
10. G. Bellussi, A. Carati, R. Millini, *Zeolites and Catalysis: Synthesis, Reactions and Applications* (Wiley, New York, 2010), p. 4492
11. C. Martinez, A. Corma, Coord. Chem. Rev. **255**, 1558 (2011)
12. M.A. Carreon, S. Li, J.L. Falconer, R.D. Noble, J. Am. Chem. Soc. **130**, 5412 (2008)
13. S.G. Li, J.G. Martinek, J.L. Falconer, R.D. Noble, Ind. Eng. Chem. Res. **44**, 3220 (2005)
14. J.F.M. Denayer, L.I. Devriese, S. Couck, J. Martens, R. Singh, P.A. Webley, G.V. Baron, J. Phys. Chem. C. **112**, 16593 (2008)
15. L. Ma, Y.S. Cheng, G. Cavataio, R.W. McCabe, L.X. Fu, J.H. Li, Chem. Eng. J. **225**, 323 (2013)
16. Y.C. Lyu, Z.M. Yu, Y. Yang, X.H. Wang, X.X. Zhao, X.M. Liu, Z.F. Yan, Fuel **243**, 398 (2019)
17. S.Z. Zhang, S.L. Chen, P. Dong, Z.Y. Ji, J.Y. Zhao, K.Q. Xu, Chin. J. Catal. **28**(10), 857 (2007)
18. P. Kortunov, S. Vasenkov, J. Karger, R. Valiullin, P. Gottschalk, M.F. Elia, M. Perez, M. Stocker, B. Drescher, G. McElhiney, C. Berger, R. Glaser, J. Weitkamp, J. Am. Chem. Soc. **127**, 13055 (2005)
19. J. Kärger, D.M. Ruthven, New J. Chem. **40**, 4027 (2016)
20. P. Mériaudeau, V.A. Tuan, F. Lefebvre, V.T. Nghiem, C. Naccache, Microporous Mesoporous Mater. **22**, 435 (1998)
21. A.K. Sinha, S. Sivasanker, Catal. Today. **49**, 293 (1999)
22. P. Liu, J. Ren, Y. Sun, Catal. Commun. **9**, 1804 (2008)
23. T. Blasco, A. Chica, A. Corma, W.J. Murphy, J. Agúndez-Rodríguez, J. Pérez-Pariente, J. Catal. **242**, 153 (2006)
24. M.Y. Kim, K. Lee, M. Choi, J. Catal. **319**, 232 (2014)
25. Y. Fan, H. Xiao, G. Shi, H. Liu, X. Bao, J. Catal. **285**, 251 (2012)
26. P. Wang, J. Zhang, G. Wang, C. Li, C. Yang, J. Catal. **338**, 124 (2016)
27. Q. Liu, H. Zuo, Q. Zhang, T. Wang, L. Ma, Chin. J. Catal. **35**(5), 748 (2014)
28. R.P. Hughes, H.A. Trujillo, J.W. Egan, A.L. Rheingold, J. Am. Chem. Soc. **122**, 2261 (2000)
29. Y.C. Lyu, Y.X. Liu, L. Xu, X.X. Zhao, Z. Liu, X.M. Liu, Appl. Surf. Sci. **401**, 57 (2017)
30. Y.C. Lyu, Z.M. Yu, Y. Yang, Y.X. Liu, X.X. Zhao, X.M. Liu, S. Mintova, Z.F. Yan, G.F. Zhao, J. Catal. **374**, 208 (2019)
31. X.D. Huang, L.J. Wang, L.D. Kong, QZh Li, Appl Catal A. **253**(2), 461 (2003)
32. Z. Chen, Y.Y. Dong, S.Y. Jiang, W.K. Lai, X.D. Yi, W.P. Fang, J. Mater. Sci. **52**, 4460 (2017)
33. F. Zhang, Y. Liu, Q. Sun, Z.F. Dai, H. Gies, Q.M. Wu, S.X. Pan, C.Q. Bian, Z.J. Tian, X.J. Meng, Y. Zhang, X.D. Zou, X.F. Yi, A.M. Zheng, L. Wang, F.S. Xiao, Chem. Commun. **53**, 4942 (2017)
34. S. Zhang, S.L. Chen, P. Dong, G. Yuan, K. Xu, Appl. Catal. A Gen. **332**, 46 (2007)
35. S. Oliver, A. Kuperman, A. Lough, G.A. Ozin, J.M. Garcés, M.M. Olken, P. Rudolf, Stud. Surf. Sci. Catal. **84**, 210 (1994)
36. O. Sel, D. Kuang, M. Thommes, B. Smarsly, Langmuir **22**, 2311 (2006)
37. K. Fang, J. Ren, Y. Sun, J. Mol, Catal. A Chem. **229**, 51 (2005)
38. X. Yang, Z. Xu, Z. Tian, H. Ma, Y. Xu, W. Qu, L. Lin, Catal. Lett. **109**, 139 (2006)
39. S.A. Khromova, A.A. Smirnov, O.A. Bulavchenko, A.A. Saraev, V.V. Kaichev, S.I. Reshetnikov, V.A. Yakovlev, Appl. Catal. A. **470**, 261 (2014)
40. Z. Hou, O. Yokota, T. Tanaka, T. Yashima, Appl. Catal. A. **253**, 381 (2003)
41. R.J.O. Mossanek, I. Preda, M. Abbate, J. Rubio-Zuazo, G.R. Castro, A. Vollmer, A. Gutiérrez, L. Soriano, Chem. Phys. Lett. **501**, 437 (2011)
42. A. Śrebowata, R. Baran, D. Lomot, D. Lisovytskiy, T. Onfroy, S. Dzwigaj, Appl. Catal. B Environ. **147**, 208 (2014)
43. L. Zhao, Y. Wang, H. An, X. Zhao, Y. Wang, Catal. Commun. **103**, 74 (2018)
44. G. Garbarino, S. Campodonico, A.R. Perez, M.M. Carnasciali, P. Riani, E. Finocchio, G. Busca, Appl. Catal. A General. **452**, 163 (2013)
45. X. Cui, Y.X. Liu, X.M. Liu, Catal. Lett. **145**, 1464 (2015)
46. Y.X. Liu, L. Xu, L.M. Zhao, L. Wei, X.M. Liu, Z.F. Yan, Catal. Sci. Technol. **6**, 3821 (2016)
47. W. Hu, H. Cong, W. Huang, Y. Huang, L.J. Chen, A.L. Pan, C.L. Xue, Light-Sci. Appl. **8**, 106 (2019)
48. M. Mujahid, C. Chen, W. Hu, Z. Wang, Y. Duan, J Sol RRL (2020). https://doi.org/10.1002/solr.201900556
49. H.S. Cho, R. Ryoo, Microporous Mesoporous Mater. **151**, 107 (2012)
50. K. Moeller, B. Yilmaz, R.M. Jacubinas, U. Mueller, T. Bein, J. Am. Chem. Soc. **133**, 5284 (2011)
51. Z.S. Yuan, W. Huang, S.T. Ma, G. Ouyang, W. Hu, W. Zhang, J. Mater. Chem. C. **7**, 5442 (2019)
52. Y.Y. Jin, Q. Sun, G.D. Qi, C. Yang, J. Xu, F. Chen, X.J. Meng, F. Deng, F.S. Xiao, Angew. Chem. Int. Ed. **26**, 9172 (2013)
53. P. Tian, X. Su, Y.X. Wang, Q.H. Xia, Y. Zhang, D. Fan, S.H. Meng, Z.M. Liu, Chem. Mater. **23**, 1406 (2011)
54. B.H. Chen, Y.N. Huang, J. Phys. Chem. C. **111**, 15236 (2007)
55. J. Yang, Z.Y. Qiu, C.M. Zhao, W.C. Wei, W.X. Chen, Z.J. Li, Y.T. Qu, J.C. Dong, J. Luo, Z.Y. Li, Y.E. Wu, Angew. Chem. Int. Ed. **57**, 14095 (2018)
56. J. Wang, W. Zhang, Y.H. Suo, Y.J. Wang, J. Porous. Mater. **25**, 1317 (2018)
57. Y.J. Wang, X.L. Dong, Y.H. Cui, S.T. Ma, Y.H. Suo, W. Zhang, J. Porous. Mater. **26**, 1279 (2019)
58. T. Blasco, A. Chica, A. Corma, W. Murphy, J. Agúndez-rodríguez, J. Pérez-pariente, J. Catal. **242**, 153 (2006)
59. C.X. Wang, Z.J. Tian, L. Wang, R.S. Xu, Q.H. Liu, W. Qu, H.J. Ma, B.C. Wang, Chemsuschem **5**, 1974 (2012)
60. J. Wang, Z.Q. Huang, W. Liu, C.R. Chang, H.L. Tang, Z.J. Li, W.X. Chen, C.J. Jia, T. Yao, S.Q. Wei, Y.E. Wu, Y.D. Li, J. Am. Chem. Soc. **139**, 17281 (2017)

61. O. Yoshio, Catal. Today. **81**, 3 (2003)
62. H.L. Coonradt, W.E. Garwood, Ind. Eng. Chem. Pro. Des. Dev. **3**(1), 38 (1964)
63. D.L. Jin, L.Y. Li, G.H. Ye, H.X. Ding, X.L. Zhao, K.K. Zhu, M.-O. Coppens, X.G. Zhou, Catal. Sci. Technol. **8**, 5044 (2018)